3D-Printed Electromagnetic Band-Gap Band-Pass Filter Based on Empty Single-Ridge Waveguide

HÉCTOR GARCÍA-MARTÍNEZ[1], (Member, IEEE),
GERMÁN TORREGROSA-PENALVA[2], (Member, IEEE), **ERNESTO ÁVILA-NAVARRO**[1],
NICOLÒ DELMONTE[3], (Member, IEEE), **LORENZO SILVESTRI**[3], (Member, IEEE),
AND MAURIZIO BOZZI[3], (Fellow, IEEE)

[1]Department of Materials Science, Optical and Electronic Technology, Universidad Miguel Hernández de Elche, 03202 Elche, Spain
[2]Department of Communication Engineering, Universidad Miguel Hernández de Elche, 03202 Elche, Spain
[3]Department of Electrical, Computer, and Biomedical Engineering, University of Pavia, 27100 Pavia, Italy

Corresponding author: Héctor García-Martínez (mhector@umh.es)

ABSTRACT In this work, a new method for the design of band-pass filters in an empty waveguide by using periodic structures is presented in a theoretical and experimental way. The proposed filter topology uses a periodic profile of two heights in the central part of an Empty Single-Ridge Waveguide (ESRW) for the generation of an Electromagnetic Band-Gap (EBG), and it provides simple unit cell design parameters to produce specific dispersion characteristics. The implementation of two band-pass filters with different fractional bandwidths (36% and 55%) and different characteristics in the rejection band is proposed, where to minimize the mismatch in the ESRW filter's passband, a tapering technique is used that follows a Kaiser distribution for the EBG. To experimentally validate the design concept, a band-pass filter with a fractional bandwidth of 55% centered on 5.45 GHz is manufactured, using a low-cost 3D printer, which allows the rapid manufacture of complex geometries at a very reduced price. The experimental results validate the simulated response of the implemented ESRW band-pass filter.

INDEX TERMS Additive manufacturing, band-pass filter, electromagnetic band-gap, empty single-ridge waveguide (ESRW), fused deposition modeling (FDM).

I. INTRODUCTION

Waveguide band-pass filters play an important role in current communication systems, because they have a series of advantages in terms of insertion loss and high-power signal handling capability [1]. Normally this type of device is implemented using simple rectangular or cylindrical resonators [2]–[5] and they are usually manufactured using numerical control milling techniques that have a high cost [6]. Currently, additive manufacturing using 3D-printing techniques has aroused great interest in different industrial sectors, moving from academic research to commercial exploitation [7], due to the ability to print complex mechanical prototypes quickly and at a reduced price as in aerospace structures [8], [9], electronic circuits [10], [11] and high frequency devices [12]–[17] for filtering applications [18]–[22].

The associate editor coordinating the review of this manuscript and approving it for publication was Qi Luo.

Taking advantage of these features can lead to faster waveguide band-pass filter development and much more complex geometries that are not feasible to implement when using traditional machining technologies. For example, in [18] band-pass filters are implemented using conical posts as a design element and in [20] they use 3D printed grooved spherical resonators to increase the rejection band of the filter.

On the other hand, periodic structures have been used in recent years for filtering applications [22], where the periodicity in the direction of propagation of electromagnetic waves results in the presence of allowed and prohibited frequency bands [23], [24], as predicted by analyzing the dispersion diagram. These characteristics make it possible to produce microwave filters with reduced dimensions, obtaining a more selective response in frequency with respect to other filters that are not periodic, providing a greater tolerance to manufacturing errors.

Recently, some articles have been published on periodic structures in Substrate Integrated Waveguide (SIW) [25], [26] and in rectangular waveguide devices [27] or Single-Ridge Waveguide (SRW) [28]. The main drawbacks in these works are the low return losses that occur when using this type of structure and the attenuation caused by the presence of the dielectric.

This work presents the design and manufacturing process of different band-pass filters in Empty Single-Ridge Waveguide (ESRW), by analyzing the dispersion diagram of a periodic unit cell. However, in this case, 3D-printing techniques are adopted to implement an empty structure that is subsequently internally metalized to reduce the attenuation caused by the dielectric. In addition, a matching technique is used to improve return losses in the entire pass band of the filters designed in a smaller size.

The paper is organized as follows. In section II, the design and analysis of the ESRW unit cell is carried out using the dispersion diagram of the Floquet modes of the infinite periodic structure, to determine the allowed and prohibited bands controlled by different design parameters. Section III presents the design of two band-pass filters with different fractional bandwidths, where tapering techniques in the different sections of the unit cells are used to yield appropriate return loss responses in the filters' pass bands. Section IV describes the manufacturing and measurement process of one of the filters implemented by means of a low-cost 3D printer, and finally the conclusions of this work are drawn in section V.

II. STUDY OF THE UNIT CELL IN A PERIODIC STRUCTURE

In order to characterize a periodic structure in the frequency domain, the dispersion diagram associated with its unit cell must be calculated. This has been done for the structure presented in this work using the eigenmode solver tool of the commercial software Ansys HFSS (see for example [29] and [30]). The unit cell is a hollow rectangular waveguide with periodic ridges on one side, as shown in Fig. 1: the (copper) metallic faces have a conductivity of $5.80 \cdot 10^7$ S/m and the inn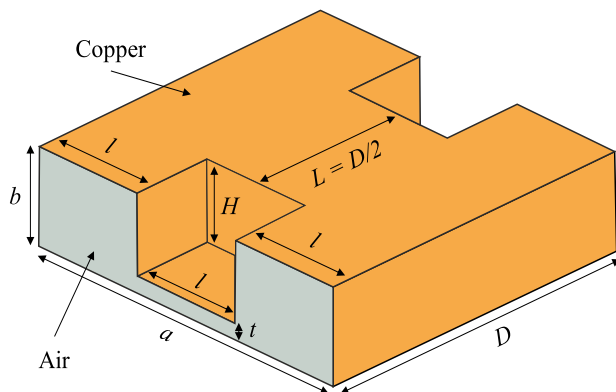er material is air (with relative dielectric permittivity $\varepsilon_r = 1.0$ and loss tangent $\tan \delta = 0$). This structure is different from the one presented in [28], where PLA (polylactic acid) is used as the inner dielectric material, incurring in the presence of considerable losses in the pass band of the final prototype.

A. DESIGN OF THE ESRW UNIT CELL

To carry out the design of the ESRW with a cutoff frequency of the fundamental mode $f_1 = 4.0$ GHz, the equations extracted from [31], [32] have been used ($a = 17.23$ mm, $b = 3.78$ mm, $t = 0.63$ mm, and $l = 5.743$ mm). The inclusion of the periodic structure in the central part of the waveguide (Fig. 1) modifies the propagation constant of the fundamental mode of the ESRW. More specifically, the cutoff frequency of the fundamental mode depends not only on the design parameters of the ESRW, but also on the dimensions of the central periodic section.

To keep the cutoff frequency of the fundamental mode at $f_1 = 4.0$ GHz, the dimensions transverse to the direction of propagation are optimized using the HFSS electromagnetic software and increased by a factor of 1.235. The final dimensions of the unit cell are $a = 21.28$ mm, $b = 3.78$ mm, $t = 0.63$ mm, and $l = 7.093$ mm.

The period D of the unit cell is determined using the equation $D = \lambda_{EBG}/4$ obtained from [22], for a central frequency of the EBG $f_{EBG} = 8.35$ GHz ($H = 3.15$ mm and $D = 20.5$ mm) so that it acts directly on the fundamental mode. Fig. 2 shows the dispersion diagram of the first five Floquet modes of the periodic structure, with the cutoff frequencies of the first two modes being $f_1 = 4.0$ GHz and $f_2 = 11.50$ GHz, respectively (and $f_B = 5.22$ GHz).
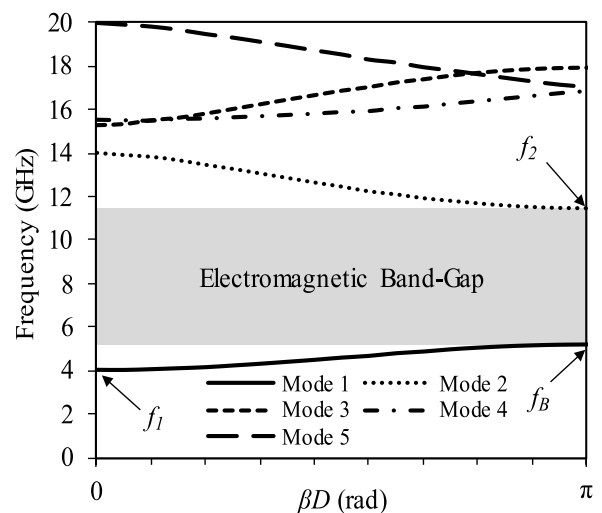

FIGURE 2. Dispersion diagram of the EBG ESRW for a step height *H* = 3.15 mm and period length *D* = 20.50 mm.

B. PARAMETRIC ANALYSIS OF THE ESRW UNIT CELL

The modification of the period D of the unit cell has a direct impact on the behavior of the ESRW dispersion diagram, in terms of the cutoff frequency of the different Floquet

FIGURE 1. Geometry of EBG ESRW unit cell.

modes in the periodic structure as well as in the single-mode bandwidth and fractional bandwidth [28], [29] (defined as $B = (f_2 − f_1)/f_1$ and $\Delta = (f_B − f_1)/\sqrt{(f_B \cdot f_1)}$ respectively).

Fig. 3 shows the dispersion diagram of the Floquet modes for different lengths of the period D of the unit cell. As can be seen in Fig. 3, for a constant height $H = 3.15$ mm, the fractional bandwidth increases significantly as the period D decreases. This is due to the fact that by reducing the period of the unit cell the forbidden band shifts to higher frequencies. It is also shown in Fig. 3 that the single-mode bandwidth increases significantly by reducing the parameter D, obtaining the maximum bandwidth with $D = 13.50$ mm. This is because the second Floquet mode begins to propagate at higher frequencies when that period is used in the unit cell. Table 1 resumes the performance of the structure when parameter D is modified. In [28] the minimum achievable bandwidth was limited by transmission losses occasioned by the excessive tan δ value of the PLA material employed for implementing the filters. In this work the empty conception of the designs permits the achievement of narrow band band-pass filters. As seen in Fig. 3 narrow band designs are attained for longer lengths D of the periodic cell. For a $\Delta = 2.5\%$ design ($f_1 = 4.0$ GHz and $f_B = 4.10$ GHz) the required unit cell length is $D = 44.50$ mm, which increases the total size of the filter.
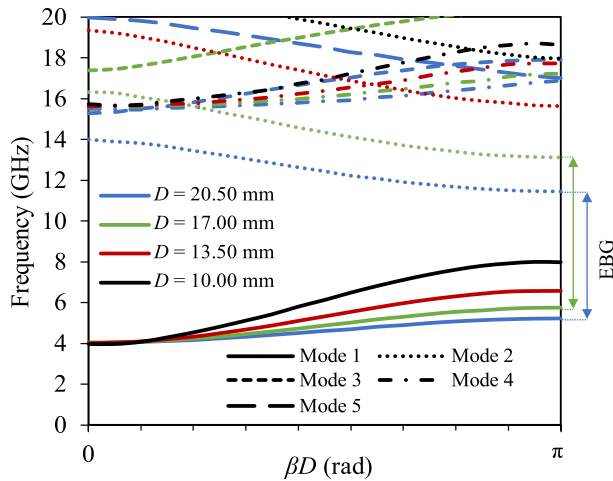

FIGURE 3. Dispersion diagram of the EBG ESRW for a step height $H = 3.15$ mm and different period length (D) of the unit cell.

TABLE 1. Cutoff frequencies of the first two modes and bandwidths for a step height $H = 3.15$ mm and different period values.

Period length D (mm)	f_1 (GHz)	f_B (GHz)	f_2 (GHz)	Δ (%)	B
20.50	4.0	5.22	11.50	26.70	1.87
17.00	4.0	5.73	13.12	36.00	2.28
13.50	4.0	6.57	15.65	50.10	2.91
10.00	4.0	7.97	15.65	70.31	2.91

On the other hand, the modification of the height H of the central section also has a direct effect on the distribution of the Floquet modes of the periodic ESRW with respect to the fractional and single-mode bandwidth. Fig. 4 shows the dispersion diagram for different values of H. It is worth highlighting that for a period $D = 13.50$ mm the fractional bandwidth of the fundamental mode decreases as H increases and the single-mode bandwidth increases until it reaches a constant value $B = 2.91$. This result has been summarized in Table 2. In this analysis l and t are kept constant to guarantee that the cutoff frequency of the fundamental mode is 4.0 GHz.
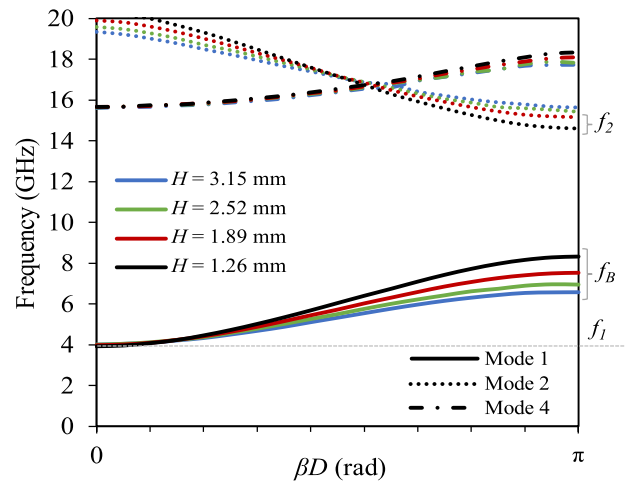

FIGURE 4. Dispersion diagram of the EBG ESRW for a period length $D = 13.50$ mm ad different height (H) of the unit cell.

TABLE 2. Cutoff frequencies of the first two modes and bandwidths for a period $D = 13.50$ mm and different step heights.

Step height H (mm)	f_1 (GHz)	f_B (GHz)	f_2 (GHz)	Δ (%)	B
3.15	4.0	6.57	15.65	50.13	2.91
2.52	4.0	6.90	15.65	55.00	2.91
1.89	4.0	7.53	15.14	64.32	2.78
1.26	4.0	8.31	14.59	74.75	2.64

C. STUDY OF THE ESRW FINITE PERIODIC STRUCTURE

In order to obtain a high rejection level in the prohibited band-gap shown in Fig. 2, a large number of unit cells (periods) must be considered [22]. However, the larger the number of periods is, the longer the structure implementation becomes. Fig. 5 shows two different finite implementation (with $D = 13.50$ mm and $H = 3.15$ mm) of the ESRW periodic structure.

The simulated (with Ansys HFSS) scattering parameters of both finite implementations are compared in Fig. 6. As expected, the rejection level in the band-gap bandwidth is higher for the longer finite implementation, while there is a good agreement between simulations and the cutoff frequency ($f_1 = 4.0$ GHz) and the band-gap frequency limits ($f_B = 6.57$ GHz and $f_2 = 15.65$ GHz).
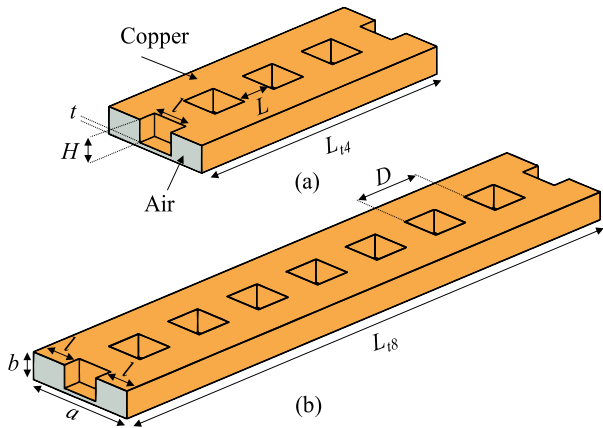
FIGURE 5. Finite implementation of the EBG ESRW with (a) 4 unit cells and (b) 8 unit cells. The dimensions indicated are: $D = 13.50$ mm, $H = 3.15$ mm, $a = 21.28$ mm, $b = 3.78$ mm, $l = 7.09$ mm, $t = 0.63$ mm, $L_{t4} = 54.0$ mm and $L_{t8} = 108.0$ mm.
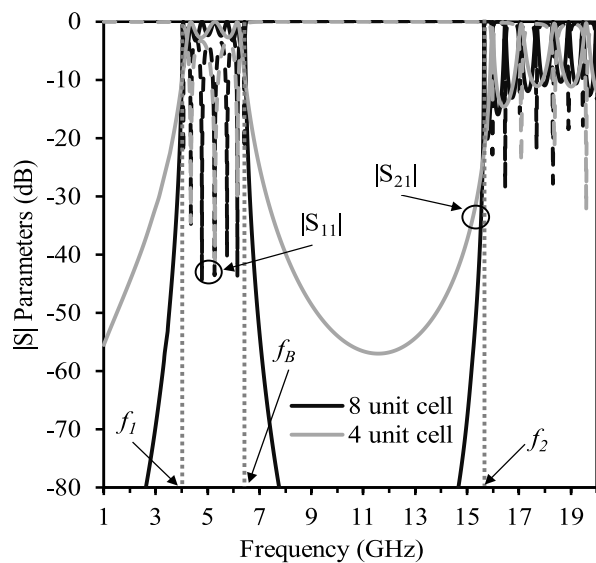

FIGURE 6. Simulated scattering parameters $|S_{21}|$ (solid line) and $|S_{11}|$ (dashed line) of two finite implementations of the EBG ESRW with 4 unit cells (grey lines) and 8 unit cells (black lines). Also shown are the lowest (f_B) and highest (f_2) frequency of the band-gap and the cut-off frequency of the fundamental mode (f_1) in the periodic structure (dotted grey lines).

III. BAND-PASS FILTERS DESIGN

After studying in section II the periodic ESRW and determining the influence of the design parameters of the empty unit cell (D and H) with respect to f_1, f_2, f_B, B and Δ, the implementation of the finite structure is performed in section III, which describes the design process for two band-pass filters with different bandwidths.

Two main drawbacks that occur when using periodic structures for filtering applications must be taken into account in the implementation of these filters as shown in Fig. 6. On the one hand, to obtain a high level of attenuation in the rejection band, a large number of unit cells must be considered, increasing the total length of the filter. On the other hand, when truncating of the periodic structure, an significant ripple appears

in the transmission and reflection coefficients of the EBG, due to the difference between the characteristic impedance of the input and output ports, Z_0, and the Bloch impedance in the periodic structure [22], leading to unacceptable levels of return losses. To solve this problem an impedance matching using a Chebyshev transformer was carried out in [28]. In this present work, to figure out this issue, tapering techniques are used [35], managing to improve the levels of return losses in the entire filter pass band and to reduce the total size of the structure compared to that presented in [28].

A. DESIGN OF A BAND-PASS FILTER WITH A FRACTIONAL BANDWIDTH OF $\Delta = 36\%$

The first designed filter, shown in Fig. 7, consists of a periodic ESRW with 8 unit cells and $\Delta = 36\%$ at a design center frequency of 4.85 GHz. The design of the filter parameters, period of the unit cell $D = 17.0$ mm and height of the central section $H = 3.15$ mm, has been carried out directly from the information provided in Fig. 3 and Tab. 1.
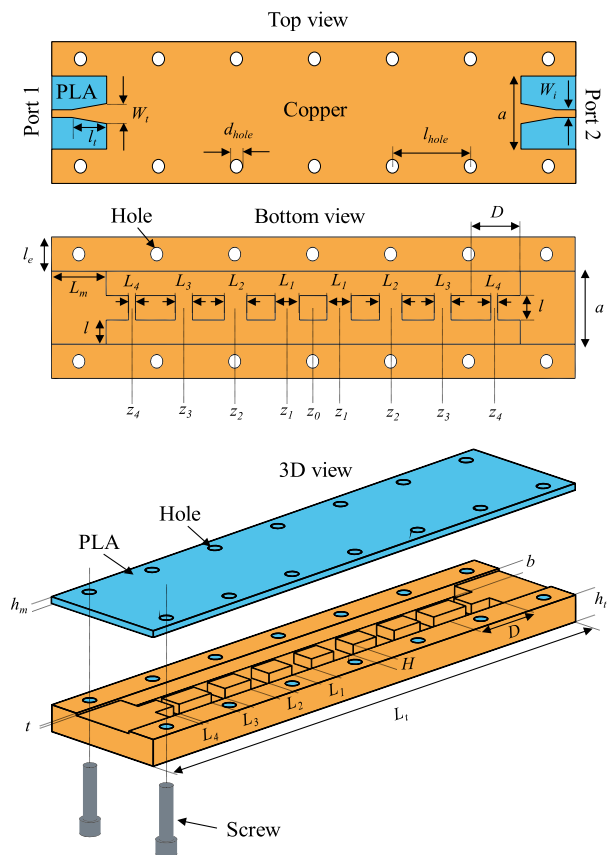

FIGURE 7. Top view, bottom view, and 3D view of the EBG ESRW band-pass filter for $\Delta = 36\%$ and 8 unit cells. EBG ESRW filter dimensions are as follows: $D = 17.0$ mm, $H = 3.15$ mm, $a = 21.28$ mm, $b = 3.78$ mm, $t = 0.63$ mm, $l = 7.09$ mm, $L_m = 18.0$ mm, $l_e = 10.0$ mm, $L_t = 172.0$ mm, $W_t = 5.87$ mm, $W_i = 2.23$ mm, $l_t = 11.49$ mm, $d_{hole} = 3.80$ mm, $l_{hole} = 25.60$ mm, $h_t = 8.0$ mm, and $h_m = 2.0$ mm.

To reduce the impedance mismatch introduced by the EBG structure, a tapering function is used, which is normally employed in Fiber Bragg Gratings (FBG) [36], [37]. The

tapering technique is applied directly by modifying the length of the central section in each period L_i of the finite structure, as shown in Fig. 7. The distribution of these lengths for each unit cell follows the next equation [38]:

$$L_i = L_{max} \times T(z_i) \qquad (1)$$

where L_i is the length of the central section of the unit cell in the i-th period, L_{max} is the maximum central length ($D/2$), $T(z)$ is the tapering function that is applied in the various unit cells and z_i is the normalized distance between the center of the i-th period and the center point of the ESRW ($z_i = z/L_{ESRW}$ where L_{ESRW} is the length and $z = 0$ its central point). The improvement in the frequency response achieved using this technique can be understood as a progressive matching of the Bloch impedance to the characteristic input and output impedances produced by the tapering function. The tapering function used follows a Kaiser window distribution given by the equation [32]:

$$T(z_i) = \frac{I_0\left(\alpha\sqrt{1-(2z_i)^2}\right)}{I_0(\alpha)} \quad with \quad \alpha = 3 \qquad (2)$$

where I_0 is the modified Bessel function of the first class and α is an arbitrary real number that determines the shape of the window.

The tapering function is applied directly on the 8 lengths (L_i) of the central section of the periods of the structure, applying equations (1) and (2). Table 3 shows the normalized coefficients of the Kaiser tapering function and the different lengths of the unit cells once applied. To make the connection of the ESRW filter in a simple way and keep losses low, a taper of length l_t has been used to match the ESRW structure to the input and output filter 50 Ω inverted microstrip lines, as shown in Fig. 7. To calculate the taper width (W_t) at the ESRW ends, the mode impedance of the fundamental mode at the center frequency of the band-pass filter ($f = 4.85$ GHz) is calculated using the HFSS simulation software.

TABLE 3. Value of taper Kaiser function and period length of each unit cell.

Section i	z_i	$T(z_i)$	L_i (mm)
1	0.0625	0.981	8.33
2	0.1875	0.839	7.13
3	0.3125	0.598	5.08
4	0.4375	0.328	2.78

The simulated filter response is shown in Fig. 8, together with the cutoff frequency f_1 of the first Floquet mode and the lower frequency f_B of the band-gap, which define the filter passband. The passband ranges from 4.0 GHz to 5.70 GHz and has a single-mode rejection band that extends up to 12.50 GHz, which coincides with the cutoff frequency f_2 of the second Floquet mode (Fig. 3). The out of band rejection is better than 30.0 dB, despite the fact that only 8 periods have been used in the finite structure. The return losses are
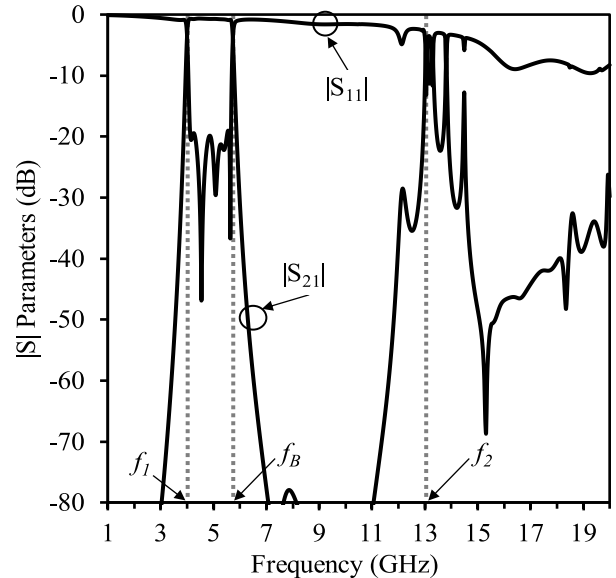

FIGURE 8. Simulated scattering parameters of the Δ = 36 % ESRW bandpass filter (black lines). Also shown are the lowest (f_B) and highest (f_2) frequency of the band-gap and the cut-off frequency of the fundamental mode (f_1) in the periodic structure (dotted grey lines).

greater than 20.0 dB in the passband and the insertion losses are less than 0.60 dB from 4.05 GHz to 5.65 GHz. The electrical characteristics considered for the PLA substrate in the simulations are $\varepsilon_r = 2.8$ and tan $\delta = 0.02$ [39], while copper is used to implement the inverted microstrip input and output lines ($\sigma = 5.80 \cdot 10^7$ S/m).

B. DESIGN OF A BAND-PASS FILTER WITH A FRACTIONAL BANDWIDTH OF Δ = 55%

The second ESRW filter implemented is shown in Fig. 9, with the same number of periods as the previous filter. In this case, the upper frequency of the passband is increased to $f_B = 6.90$ GHz, Δ = 55% for a central frequency of 5.45 GHz. The design parameters of the band-pass filter (which ranges from f_1 and f_B) can be extracted again from Fig. 4 and Tab. 2, being the length of the unit cell $D = 13.50$ mm and the height of the central section $H = 2.52$ mm. To carry out the matching in the filter passband and reduce the ripple introduced by the EBG, the same tapering function of the previous filter is used, modifying the length of the central section of the 8 periods for each different unit cell, applying equations (1) and (2). The central lengths of the different sections once calculated and optimized are: $L_1 = 6.62$ mm, $L_2 = 5.66$ mm, $L_3 = 4.03$ mm and $L_4 = 2.16$ mm.

Finally, a taper of length l_t is included at the input and output ports of the ESRW as shown in Fig. 7, to match the structure to the 50 Ω inverted microstrip transmission lines.

The simulated filter response is shown in Fig. 10, as well as the cutoff frequency f_1 of the first Floquet mode and the lower frequency f_B of the band-gap. The filter's passband ranges from 4.0 GHz to 6.90 GHz, which is larger than the previous filter and has a single-mode rejection band that extends up
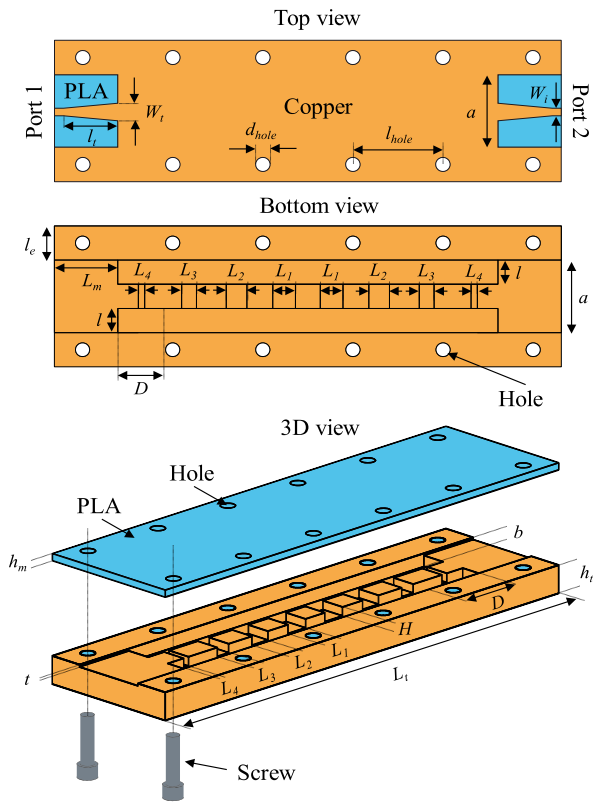
FIGURE 9. Top view, bottom view, and 3D view of the EBG ESRW band-pass filter for $\Delta = 55\%$ and 8 unit cells. EBG ESRW filter dimensions are as follows: $D = 13.5$ mm, $H = 2.52$ mm, $a = 21.28$ mm, $b = 3.78$ mm, $t = 0.63$ mm, $l = 7.09$ mm, $L_m = 18.0$ mm, $l_e = 10.0$ mm, $L_t = 144.0$ mm, $W_t = 5.04$ mm, $W_i = 2.23$ mm, $l_t = 15.50$ mm, $d_{hole} = 3.80$ mm, $l_{hole} = 25.60$ mm, $h_t = 8.0$ mm, and $h_m = 2.0$ mm.

to 16.0 GHz with out of band rejection better than 30.0 dB. Return loss is larger than 20 dB throughout the passband while insertion loss is less than 0.6 dB from 4.05 GHz to 6.85 GHz.

IV. 3D-PRINTED FILTER PROTOTYPING

To demonstrate the practical feasibility of the theoretical analysis of ESRW band-pass filters described in the previous sections, the ESRW filter with a fractional bandwidth of $\Delta = 55\%$ shown in Fig. 9 was manufactured and measured. The filter is divided into two different parts that were implemented individually (Fig. 11): the upper part (top view) formed by the inverted microstrip transmission line and the flat face of the ESRW, and the base (bottom view) which is formed by the ESRW itself. As shown in Fig. 11 the two pieces were manufactured using PLA filament and a low-cost 3D printer BQ's Prusa i3 Hephestos with a resolution of 0.015 mm in the XY axes and a 0.4 mm diameter nozzle.

The metallization of the two pieces of PLA that make up the ESRW filter is carried out following a multi-step process. First, a conductive copper spray (MG Chemicals) is applied over the entire surface of the PLA parts with a thickness of $\sim 20\ \mu$m. Second, an LPKF Protomat S42 numerical control milling machine is used to selectively remove the metal coating and make the transitions from the ESRW to the
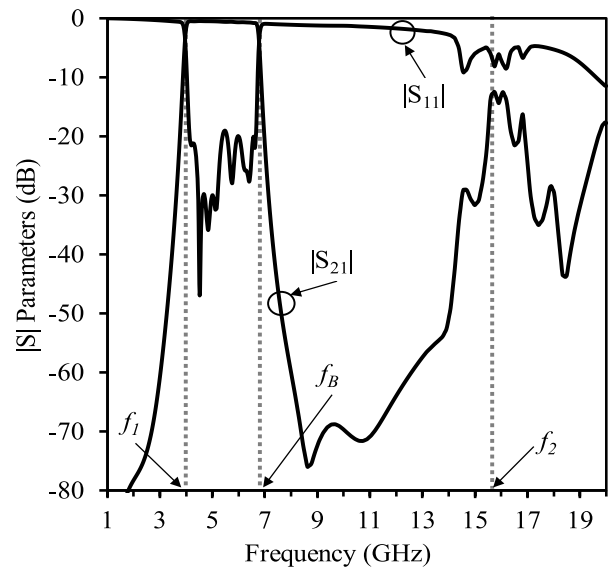

FIGURE 10. Simulated scattering parameters of the $\Delta = 55\%$ ESRW band-pass filter (black lines). Also shown are the lowest (f_B) and highest (f_2) frequency of the band-gap and the cut-off frequency of the fundamental mode (f_1) in the periodic structure (dotted grey lines).
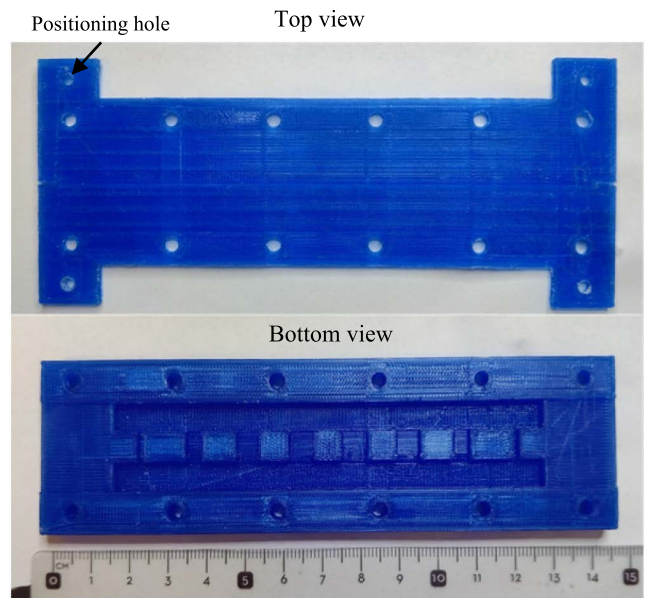

FIGURE 11. Photograph of the two 3D-printed parts of the $\Delta = 55\%$ ESRW filter using PLA before metallization process.

inverted microstrip lines of the filter's input and output ports, with the help of the positioning holes shown in Fig. 11 (top view). Finally, a conventional copper electroplating process is carried out to increase the thickness of the copper to $\sim 35\ \mu$m (with an accuracy of $\pm 5\ \mu$m) and the conductivity of the 3D-printed parts. The final result after metallization of the two pieces of the ESRW filter for a bandwidth $\Delta = 55\%$ is shown in Fig. 12.

On the other hand, in order to incorporate the SMA connectors to the input and output ports of the ESRW filter, two grooves had to be left in the PLA in the central part of the inverted microstrip line to be able to correctly accommodate
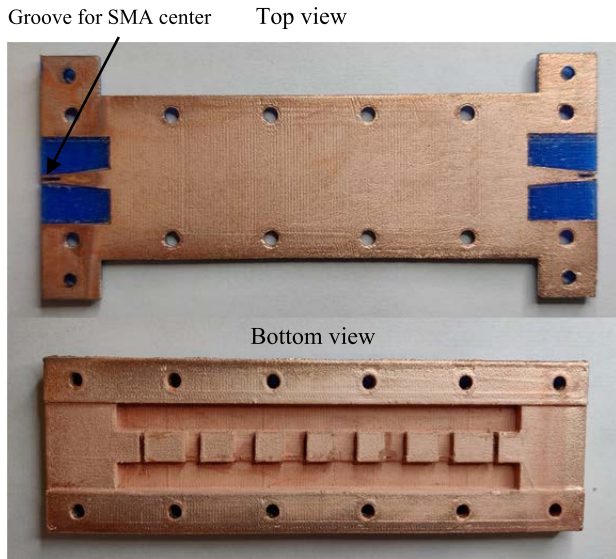
FIGURE 12. Photograph of the final ESRW filter prototype after the manufacturing process.
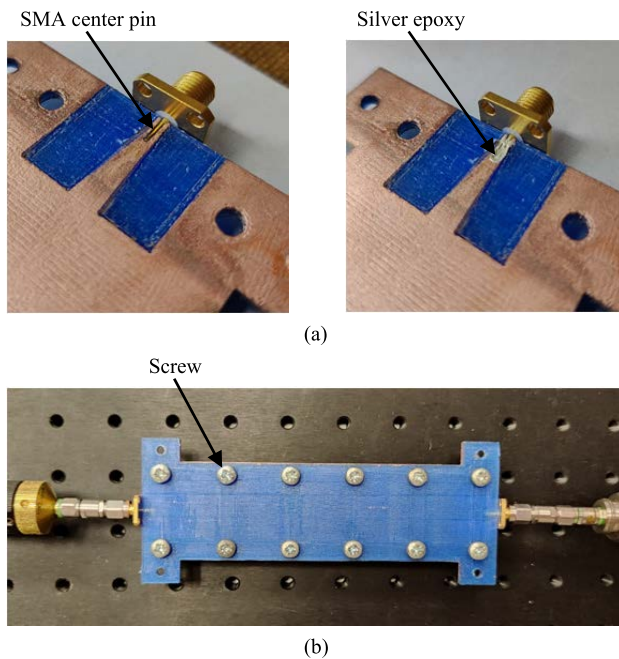

FIGURE 13. (a) Photograph of the connection and soldering process of the SMA connector to the inverted microstrip line. (b) Measurement setup.

the central conductor of the coaxial connector, as shown in Fig. 12. In Fig. 13(a) the process of connecting the SMA connector to the groove in the inverted microstrip line is shown, where a silver epoxy (RS PRO) is included to electrically join the SMA inner conductor to the transmission line. Fig. 13(b) presents the final prototype, including the connection of the screws to adjust the filter structure and the input and output ports of the vector network analyzer.

The S-parameters of the manufactured filter were measured using the Agilent PNA E8363C Vector Network Analyzer. The simulations and measurements of the
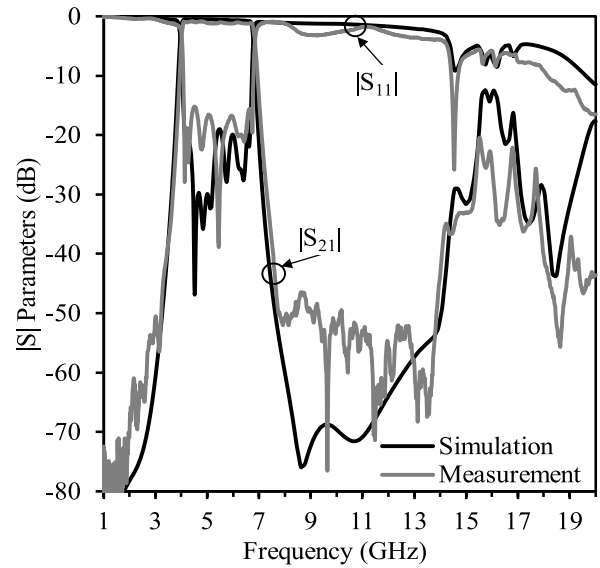

FIGURE 14. Simulated (black lines) and measured (grey lines) responses scattering parameters of the Δ = 55 % ESRW band-pass filter.

S-parameters of the fabricated device are compared in Fig. 14, showing good agreement over the entire frequency range. The measured frequencies of the filter passband and rejection band are f_1 = 4.0 GHz, f_B = 6.79 GHz and f_2 = 15.80 GHz, which are very similar to those simulated with HFSS f_1 = 4.0 GHz, f_B = 6.80 GHz and f_2 = 15.80 GHz (this small deviation from the EBG cutoff frequency could be due to small variations in the filter manufacturing process in the 3D printer and to the tolerance in the PLA surface metallization process). The measured insertion loss in the filter passband is 0.89 dB, very close to the insertion loss of 0.50 dB obtained in the simulation (this variation could be due to the losses introduced by the SMA connectors that are not included in the HFSS simulation). Insertion losses are 3.5 dB better than in the PLA filter implemented in [28] (both filters with similar design center frequency and bandwidth). The return loss measured in the filter passband is better than 16.50 dB, which confirms the matching approach followed in the filter design (the small disagreement could be due to minor variations in the relative permittivity of the PLA or manufacturing errors in the printing of the filter and in the milling process of the inverted microstrip).

V. CONCLUSION
In this work, a simple topology for the design of band-pass filters in an empty waveguide is presented through the use of periodic structures. The design process for band-pass filters is based on including an EBG in an ESRW, using two different heights in the central section of the waveguide in order to produce the desired frequency response. The analysis of the dispersion diagram of the unit cell of the periodic structure allows to study the different design parameters of the filter frequency response, providing total control over the required specifications of the filter. The cutoff frequencies of the passband and the forbidden band are mainly determined by

the height of the center section and the period of the periodic structure, respectively.

To validate the configuration and the proposed design method, two band-pass filters with different fractional and single-mode bandwidths are presented, improving the response of the reflection coefficient in the passband by using a Kaiser EBG distribution in the different lengths of the central sections of the unit cells, providing excellent transmission in the ESRW filter passband. Finally, a band-pass filter with a 55% fractional bandwidth is manufactured using a low-cost 3D-printing technology and an electroplating process to metallize the structure. The measured filter response is consistent with electromagnetic simulation and provides good passband and rejection band performance through the use of a simple-to-design structure with low insertion losses and high return losses.

The results presented in this work are very promising and open a wide range of possibilities for 3D-printing technology to develop and design microwave filters in an easy way in ESRW that present: very low transmission losses, wide working bandwidths and rejection, with a very reduced cost and manufacturing time.

REFERENCES

[1] I. Arregui, F. Teberio, I. Arnedo, J. M. Percaz, P. Martin-Iglesias, T. Lopetegi, and M. A. G. Laso, "High-power filter design in waveguide technology: Future generation of waveguide satellite filters in payloads handling increasing bit rates and numbers of channels," *IEEE Microw. Mag.*, vol. 21, no. 6, pp. 46–57, Jun. 2020.

[2] Z.-C. Guo, L. Zhu, and S.-W. Wong, "Synthesis of transversal bandpass filters on stacked rectangular *H*-plane waveguide cavities," *IEEE Trans. Microw. Theory Techn.*, vol. 67, no. 9, pp. 3651–3660, Sep. 2019.

[3] A. E. Atia and A. E. Williams, "Narrow-bandpass waveguide filters," *IEEE Trans. Microw. Theory Techn.*, vol. 20, no. 4, pp. 258–265, Apr. 1972.

[4] S. Afridi, U. Ahmed, A. R. Gilal, J. Jaafar, I. A. Aziz, and M. Y. Sandhu, "High stop band rejection for ceramic loaded waveguide filters," *IEEE Access*, vol. 8, pp. 109309–109314, 2020.

[5] A. A. San-Blas, M. Guglielmi, J. C. Melgarejo, A. Coves, and V. E. Boria, "Design procedure for bandpass filters based on integrated coaxial and rectangular waveguide resonators," *IEEE Trans. Microw. Theory Techn.*, vol. 68, no. 10, pp. 4390–4404, Oct. 2020.

[6] Y. Shi, J. Zhang, M. Zhou, W. Feng, B. Cao, and W. Che, "Miniaturized W-band gap waveguide bandpass filter using the MEMS technique for both waveguide and surface mounted packaging," *IEEE Trans. Circuits Syst. II, Exp. Briefs*, vol. 66, no. 6, pp. 938–942, Jun. 2019.

[7] W. Gao, Y. Zhang, D. Ramanujan, and K. Ramani, "The status, challenges, and future of additive manufacturing in engineering," *Comput.-Aided Des.*, vol. 69, pp. 65–89, Dec. 2015.

[8] U. Fasel, D. Keidel, L. Baumann, G. Cavolina, M. Eichenhofer, and P. Ermanni, "Composite additive manufacturing of morphing aerospace structures," *Manuf. Lett.*, vol. 23, pp. 85–88, Jan. 2020.

[9] R. Elhajjar, *Advanced Manufacturing Aerospace Components Structural: Fabrication Reliability*, Madison, WI, USA: Society of Automotive Engineers, 2017.

[10] E. MacDonald, R. Salas, D. Espalin, M. Perez, E. Aguilera, D. Muse, and R. B. Wicker, "3D printing for the rapid prototyping of structural electronics," *IEEE Access*, vol. 2, pp. 234–242, 2014.

[11] C. Kim, D. Espalin, M. Liang, H. Xin, A. Cuaron, I. Varela, E. Macdonald, and R. B. Wicker, "3D printed electronics with high performance, multi-layered electrical interconnect," *IEEE Access*, vol. 5, pp. 25286–25294, 2017.

[12] R. Bahr, B. Tehrani, and M. M. Tentzeris, "Exploring 3-D printing for new applications: Novel inkjet- and 3-D-printed millimeter-wave components, interconnects, and systems," *IEEE Microw. Mag.*, vol. 19, no. 1, pp. 57–66, Jan. 2018.

[13] E. Massoni, L. Silvestri, G. Alaimo, S. Marconi, M. Bozzi, L. Perregrini, and F. Auricchio, "3-D printed substrate integrated slab waveguide for single-mode bandwidth enhancement," *IEEE Microw. Wireless Compon. Lett.*, vol. 27, no. 6, pp. 536–538, Jun. 2017.

[14] F. Oktafiani, E. Y. Hamid, and A. Munir, "Wideband dual-polarized 3D printed quad-ridged horn antenna," *IEEE Access*, vol. 10, pp. 8036–8048, 2022.

[15] F. Cai, Y.-H. Chang, K. Wang, C. Zhang, B. Wang, and J. Papapolymerou, "Low-loss 3-D multilayer transmission lines and interconnects fabricated by additive manufacturing technologies," *IEEE Trans. Microw. Theory Techn.*, vol. 64, no. 10, pp. 3208–3216, Oct. 2016.

[16] E. Marquez-Segura, S.-H. Shin, A. Dawood, N. M. Ridler, and S. Lucyszyn, "Microwave characterization of conductive PLA and its application to a 12 to 18 GHz 3-D printed rotary vane attenuator," *IEEE Access*, vol. 9, pp. 84327–84343, 2021.

[17] Y. Zhang, F. Zhang, Y. Gao, J. Xu, C. Guo, and X. Shang, "3D printed waveguide step-twist with bandpass filtering functionality," *Electron. Lett.*, vol. 56, no. 11, pp. 527–528, 2020.

[18] E. Lopez-Oliver, C. Tomassoni, L. Silvestri, M. Bozzi, L. Perregrini, S. Marconi, G. Alaimo, and F. Auricchio, "3-D-printed compact band-pass filters based on conical posts," *IEEE Trans. Microw. Theory Techn.*, vol. 69, no. 1, pp. 616–628, Jan. 2021.

[19] J. Li, C. Guo, L. Mao, J. Xiang, G.-L. Huang, and T. Yuan, "Monolithically 3-D printed hemispherical resonator waveguide filters with improved out-of-band rejections," *IEEE Access*, vol. 6, pp. 57030–57048, 2018.

[20] A. Vallecchi, D. Cadman, W. G. Whittow, J. Vardaxoglou, E. Shamonina, and C. J. Stevens, "3-D printed bandpass filters with coupled vertically extruded split ring resonators," *IEEE Trans. Microw. Theory Techn.*, vol. 67, no. 11, pp. 4341–4352, Nov. 2019.

[21] F. Zhang, C. Guo, Y. Zhang, Y. Gao, B. Liu, and M. Shu, "A 3-D printed bandpass filter using TM_{211}-mode slotted spherical resonators with enhanced spurious suppression," *IEEE Access*, vol. 8, pp. 213215–213223, 2020.

[22] F. Martin, *Artificial Transmission Lines for RF and Microwave Applications*. Hoboken, NJ, USA: Wiley, 2015.

[23] S. Moscato, R. Moro, M. Pasian, M. Bozzi, and L. Perregrini, "Two-material ridge substrate integrated waveguide for ultra-wideband applications," *IEEE Trans. Microw. Theory Techn.*, vol. 63, no. 10, pp. 3175–3182, Oct. 2015.

[24] Á. Coves, S. Marini, B. Gimeno, and V. Boria, "Full-wave analysis of periodic dielectric frequency-selective surfaces under plane wave excitation," *IEEE Trans. Antennas Propag.*, vol. 60, no. 6, pp. 2760–2769, Jun. 2012.

[25] L. Silvestri, E. Massoni, C. Tomassoni, A. Coves, M. Bozzi, and L. Perregrini, "Substrate integrated waveguide filters based on a dielectric layer with periodic perforations," *IEEE Trans. Microw. Theory Techn.*, vol. 65, no. 8, pp. 2687–2697, Aug. 2017.

[26] D. Lopez, A. Coves, E. Bronchalo, G. Torregrosa, and M. Bozzi, "Practical design of a band-pass filter using EBG SIW technology," in *Proc. 48th Eur. Microw. Conf. (EuMC)*, Madrid, Spain, Sep. 2018, pp. 77–80.

[27] H. Garcia-Martinez, G. Torregrosa-Penalva, E. Avila-Navarro, A. Coves-Soler, and E. Bronchalo, "Complex structures in microwave circuits by using additive manufacturing techniques," in *Proc. 49th Eur. Microw. Conf. (EuMC)*, Paris, France, Oct. 2019, pp. 782–785.

[28] H. Garcia-Martinez, E. Avila-Navarro, G. Torregrosa-Penalva, N. Delmonte, L. Silvestri, S. Marconi, G. Alaimo, F. Auricchio, and M. Bozzi, "Design and fabrication of a band-pass filter with EBG single-ridge waveguide using additive manufacturing techniques," *IEEE Trans. Microw. Theory Techn.*, vol. 68, no. 10, pp. 4361–4368, Oct. 2020.

[29] T. K. Mealy, I. A. Eshrah, and T. M. Abuelfadl, "Solution of periodically loaded waveguides using the eigenmode projection technique," in *IEEE MTT-S Int. Microw. Symp. Dig.*, San Francisco, CA, USA, May 2016, pp. 1–4.

[30] S. J. Lavdas, C. S. Lavranos, and G. A. Kyriacou, "Periodic structures eigenanalysis incorporating the floquet field expansion," in *Proc. Int. Conf. Electromagn. Adv. Appl.*, Turin, Italy, Sep. 2011, pp. 1253–1256.

[31] W. J. R. Hoefer and M. N. Burton, "Closed-form expressions for the parameters of finned and ridged waveguides," *IEEE Trans. Microw. Theory Techn.*, vol. 30, no. 12, pp. 2190–2194, Dec. 1982.

[32] S. Hopfer, "The design of ridged waveguides," *IRE Trans. Microw. Theory Techn.*, vol. 3, no. 5, pp. 20–29, Oct. 1955.

[33] D. M. Pozar, *Microwave Engineering*. Indianapolis, IN, USA: Wiley, 1998.

[34] M. Bozzi, S. A. Winkler, and K. Wu, "Broadband and compact ridge substrate-integrated waveguides," *IET Microw., Antennas Propag.*, vol. 4, no. 11, pp. 1965–1973, 2010.

[35] S. Y. Huang and Y. H. Lee, "Tapered dual-plane compact electromagnetic bandgap microstrip filter structures," *IEEE Trans. Microw. Theory Techn.*, vol. 53, no. 9, pp. 2656–2664, Sep. 2005.

[36] A. Syahriar, D. Astharini, and A. H. Lubis, "The effects of apodization profile on uniform fiber Bragg gratings," in *Proc. 9th Int. Conf. Telecommun. Syst. Services Appl. (TSSA)*, Bandung, Indonesia, Nov. 2015, pp. 1–6.

[37] S. Maiti and V. Singh, "Performance analysis of apodized fiber Bragg gratings for sensing applications," *Silicon*, vol. 14, no. 2, pp. 581–587, Nov. 2020.

[38] N. C. Karmakar and M. N. Mollah, "Investigations into nonuniform photonic-bandgap microstripline low-pass filters," *IEEE Trans. Microw. Theory Techn.*, vol. 51, no. 2, pp. 564–572, Feb. 2003.

[39] H. García-Martínez, E. Ávila-Navarro, G. Torregrosa-Penalva, A. Rodríguez-Martínez, C. Blanco-Angulo, and M. A. D. L. de la Casa-Lillo, "Low-cost additive manufacturing techniques applied to the design of planar microwave circuits by fused deposition modeling," *Polymers*, vol. 12, no. 9, p. 1946, Aug. 2020.

NICOLÒ DELMONTE (Member, IEEE) was born in Broni, Italy, in 1992. He received the bachelor's degree in electronics and computer engineering and the master's degree in electronic engineering from the University of Pavia, Italy, in February 2015 and September 2017, respectively, and the Ph.D. degree from the Microwave Laboratory research group of the University of Pavia, in April 2021. He is currently working as a Postdoctoral Researcher with the University of Pavia. His main research topics include passive microwave components in substrate integrated waveguide (SIW) technology, 3D printed electromagnetic devices, and antenna array development.

HÉCTOR GARCÍA-MARTÍNEZ (Member, IEEE) was born in Albatera, Spain, in 1991. He received the M.S. degree in telecommunication engineering and the Ph.D. degree in industrial and telecommunication technologies from the Miguel Hernández University of Elche (UMH), Elche, Spain, in 2016 and 2021, respectively.

He was a Visiting Scholar with the Microwave Laboratory, University of Pavia, Pavia, Italy, in 2019. He is currently an Assistant Professor with the Department of Materials Science, Optics and Electronic Technology, UMH, where he is also a Research Fellow with the Radio frequency System Group. His research interests include the design of passive and active microwave circuits in complex structures through 3-D additive manufacturing techniques and the analysis of biological materials using microwave devices.

LORENZO SILVESTRI (Member, IEEE) was born in Novara, Italy, in July 1987. He received the M.Sc. degree in electronic engineering–telecommunication system curriculum and the Ph.D. degree in electronic, electrical, and computer engineering from the University of Pavia, Pavia, Italy, in 2014 and 2019, respectively.

In 2014, he was a recipient of a one year post-graduate scholarship at the University of Pavia, working on passive substrate integrated waveguide (SIW) component. After the Ph.D. until September 2020, he held a postdoctoral position with the University of Pavia, working on the design of reconfigurable SIW antennas. He is currently a Researcher at the University of Pavia. In 2015, he was a co-recipient for the Best Paper Award at 15th Mediterranean Microwave Symposium (MMS 2015).

GERMÁN TORREGROSA-PENALVA (Member, IEEE) received the Telecommunications Engineering and Ph.D. degrees from the Universidad Politécnica de Madrid (UPM), Madrid, Spain, in 1999 and 2004, respectively. In October 2002, he joined the Miguel Hernández University of Elche, Elche, Spain, where he is currently an Associate Professor with the Department of Communications Engineering. His research interests include the study of electron discharges in microwave components, sensor networks using microwave photonics, thermal and electrical characterization of microwave power amplifiers, additive manufacturing of high-frequency devices, and the design of microwave circuits and subsystems.

MAURIZIO BOZZI (Fellow, IEEE) received the Ph.D. degree in electronics and computer science from the University of Pavia, in 2000.

He held research positions with various universities, including the Technische Universität Darmstadt, Germany; the Universitat de Valencia, Spain; and the École Polytechnique de Montréal, Canada. In 2002, he joined the University of Pavia, where he is currently a Full Professor. He was also a Guest Professor with Tianjin University, China, and a Visiting Professor with the Gdańsk University of Technology, Poland. He has authored or coauthored more than 150 journal articles and 340 conference papers, and the book *Microstrip Lines and Slotlines* (Artech House, 2013). His main research interests include computational electromagnetics, the substrate integrated waveguide technology, and the use of novel materials and fabrication technologies for microwave circuits.

Prof. Bozzi is an Elected Member of the Administrative Committee of the IEEE Microwave Theory and Techniques Society (MTT-S) for years 2017–2022 and the current MTT-S Treasurer. He received several awards, including the 2014 Premium Award for Best Paper in *Electronics Letters* and the 2015 Premium Award for Best Paper in *IET Microwaves, Antennas & Propagation*. He was the General Chair of the various international conferences, including the IEEE IMWS-AMP 2017, IEEE NEMO 2014, and IEEE IMWS 2011, and the General TPC Chair of EuMW 2022. He is a Track Editor of the IEEE Transactions on Microwave Theory and Techniques.

ERNESTO ÁVILA-NAVARRO received the M.Sc. degree in telecommunication engineering from the Polytechnic University of Valencia, Spain, in 1998, and the Ph.D. degree from the Miguel Hernández University of Elche, in Spain 2008, for a work on planar antennas for specific personal wireless applications.

In 2000, he joined the Miguel Hernández University of Elche, where he is currently an Associate Professor with the Department of Materials Science, Optics and Electronic Technology. His current research interests include printed antennas, passive and active microwave devices, bioelectronics, and microwave imaging systems for tumor detection.

• • •